Lattice Boltzmann Method for Simulation of Shale Gas Transport in Kerogen

Ebrahim Fathi, SPE, West Virginia University, and **I. Yucel Akkutlu,** SPE, Texas A&M University

Summary

Fluid mechanics of natural gas in organic-rich shale involves nanoscale phenomena that could lead to potential non-Darcy effects during gas production. In general, these are low-Reynolds-number and noncontinuum effects and, more importantly, pore-wall-dominated multiscale effects. In this study, we introduce a new lattice Boltzmann method (LBM) to investigate these effects numerically in simple pore geometries. The standard method was developed in the 1980s to overcome the weaknesses of lattice gas cellular automata and has emerged recently as a powerful tool to solve fluid dynamics problems, in particular in the areas of micro- and nanofluidics. The new approach takes into account molecular-level interactions by use of adsorptive/cohesive forces among the fluid particles and defining a Langmuir-slip boundary condition at the organic pore walls. The model allows us to partition mass transport by the walls into two components: slippage of free gas molecules and hopping (or surface transport) of the adsorbed gas molecules. By use of the standard 2D D2Q9 lattice, low-Reynolds-number gas dynamics is simulated in a 100-nm model organic capillary and later in a bundle of smaller-sized organic nanotubes. The results point to the existence of a critical Knudsen-number value for the onset of laminar gas flow under typical shale-gas-reservoir pressure conditions. Beyond this number, the predicted velocity profile shows that the mechanisms of slippage and surface transport could lead to molecular streaming by the pore walls, which enhances the gas transport in the organic nanopores. The work is important for development of new-generation shale-gas-reservoir flow simulators, and it can be used in the laboratory for organic-rich-shale characterization.

Introduction

Advanced microscopy and image analysis techniques have been used to investigate pore scale characteristics of resource shale formations (Loucks et al. 2009; Wang and Reed 2009; Sondergeld et al. 2010; Kang et al. 2011; Ambrose et al. 2012). A popular approach today is focused ion-beam scanning electron microscopy. 2D scanning electron micrographs at micron scale reveal the presence of finely dispersed organic porous material, widely known as kerogen, imbedded within the inorganic matrix. A significant portion of the pores associated with gas storage is found within these kerogen pockets (Kang et al. 2011) that are 200–500 nm in size. Kerogen pores are micropores with sizes less than 2.0 nm and mesopores with sizes in the range 2 to 50 nm. Although some larger pores may exist, the average kerogen pore size is typically below 10 nm (Adesida et al. 2011). The range of pore sizes shows that the organic-rich shale can, in general, be considered a naturally occurring nanoporous material. At this scale, the continuum assumption of fluid flow may break down and the Navier-Stokes equations with no-slip boundaries may not be valid. This means that the classical approach to modeling gas flow that is based on Darcy's law may not be suitable for reservoir flow simulation. In this paper a new simulation approach is presented to study the pore size dependency of gas transport in organic nanoporous materials and to answer some of these questions. The approach considers natural gas as a swarm of particles colliding and streaming in model capillaries represented by a 2D discrete square lattice. Under certain initial and boundary (nonequilibrium) conditions, the particles interact intrinsically among themselves and with the capillary walls, whereas they collectively obey the Boltzmann transport equation. During the streaming/collision/relaxation processes, these interactions manifest a microcosm of viscous-flow behavior inside the capillary. The lattice space and time evolution of the fluid particles is then studied in terms of the predicted particle velocities at the nodes across the capillary. The simulation approach can handle arbitrarily complex pore geometries in a fairly straightforward way, and, because of its intrinsic kinetic nature, it can also handle the high-Knudsen number regime where both macroscopic dynamics and microscopic statistics are important.

Knudsen number (Kn) is used during a discussion on the validity of continuum equations. It is traditionally defined as the ratio of the mean free path of molecules (λ) to the macroscopic length scale of the pores (H): $Kn = \lambda / H$. In Roy et al. (2003), different flow regimes are described including continuum flow, slip flow, transition (or Knudsen) flow, and free-molecule flow, with the Knudsen number in the ranges of $Kn < 10^{-3}$, $10^{-3} < Kn < 10^{-1}$, $10^{-1} < Kn < 10$, and $10 < Kn$, respectively. On the basis of this argument, our group recently showed (Kang et al. 2011) that the flow of gas inside organic pores in shale is mainly in the Knudsen-flow or in the free molecule-flow regimes where the continuum equations are not valid. Consequently, to predict the gas flow dynamics requires different modeling and simulation techniques. Our group has been using molecular modeling and simulation techniques that are suitable to investigate thermodynamics of natural gases (e.g., methane, ethane, nitrogen, and carbon dioxide) in model pores under equilibrium conditions (see, for example, Adesida et al. 2011; Diaz-Campos 2010; Kang et al. 2011). These particle-based microscopic simulation approaches, however, involve numerical solutions to the many-body problem and are too costly when gas is considered in a large nano-tube (with size greater than 10 nm) or in a 3D kerogen pore network. Today, molecular dynamics simulations typically include a few thousand molecules in an organic nanopore (with size less than 10 nm) and use femtosecond (10^{-15} seconds) timesteps. On the other hand, the Monte Carlo simulations of a similar problem converge to thermodynamic equilibrium only after hundreds of thousands of cycles of random trial moves. These obviously point to extremely high computational costs for this study. Furthermore, there exist technical difficulties in simulating molecular behavior under nonequilibrium conditions, when, for example, a net molecular flux exists at the inlet and outlet of an organic nanopore. Even though these methods have allowed us make significant progress in our understanding of the thermodynamics of fluids in shales, a new approach is necessary to study solid/gas interaction under nonequilibrium conditions with a particular interest on mass transport at the mesoscale.

The LBM has strong theoretical background and some numerical advantages that made it a powerful tool to simulate various fluid dynamics at different scales from the continuum-level viscous-flow problem to heat and mass transport through microchannels (Succi 2001; Nie et al. 2002; Myong et al. 2005; Chen 2007). LBM is fundamentally a mesoscopic approach initially developed as an alternative to the lattice gas cellular automata. Consistent with the kinetic theory of gases, in this method the gas is considered to be composed of interacting fluid particles streaming in

This paper (SPE 146821) was accepted for presentation at the SPE Annual Technical Conference and Exhibition, Denver, Colorado, USA, 30 October–2 November 2011, and revised for publication. Original manuscript received for review 28 June 2011. Revised paper received for review 29 June 2012. Paper peer approved 6 July 2012.

space and having elastic collisions of spherical particles. The particles do not represent atoms or molecules; instead, they are coarse particles (or coarse grains) although they are typically considered much smaller than the fluid particles of the continuum mechanics. The microscopic physics of fluid flow is considered with much less computational cost in comparison to molecular dynamics and Monte Carlo simulations; in fact, the cost is comparable with that of common Navier-Stokes solvers (Chen and Doolen 1998; Myong et al. 2006). The lattice Boltzmann equation can be obtained by discretizing the Enskog equation in phase space and time, or directly from the continuous Boltzmann equation (Ho and Tai 1998). The solution at the limiting case (i.e., small Knudsen numbers) converges to the Navier-Stokes solution of continuum equations, although, because of its kinetic nature, it can also be used to simulate transition flow and free molecular transport at high Knudsen numbers. These features make LBM an efficient and predictive tool suitable for this study.

Currently, more-sophisticated lattice Boltzmann models are being developed to simulate multicomponent and multiphase fluid systems (Shan and Chen 1993; Martys and Chen 1996; He and Doolen 2002). In more-specific applications, LBM has been used to capture the behavior of nonideal gases and inhomogeneous fluids. The method has also been very powerful to simulate the fluid flow in porous media with complex boundary conditions (Dardis and McCloskey 1998; Sukop and Or 2004; Ramstad et al. 2010). It has been used to simulate interfacial dynamics caused by fluid/fluid or fluid/solid interactions (e.g., surface tension, cavitation, or adsorption) in porous materials, where capillarity may play a critical role in mass transport.

Implementing intricate boundary conditions associated with tube or pore walls has been a focus for the LBM development (Martys and Chen 1996; Or and Tuller 2002; Sukop and Or 2005). Slip boundary conditions have been a subject of research for more than a decade where gas flow in microelectromechanical systems is considered (Ho and Tai 1998). The most important characteristic of gas flow in these microsystems is the slip motion at the surface of the solid, which increases with the Knudsen number. Different types of boundary conditions have been considered to model the slip velocity at solid surfaces. Some involved modifications to common bounce-back boundaries, such as the halfway bounce-back rule developed by Nie et al. (2002), where the slip velocity at large Knudsen number is approximated by a parabolic velocity distribution with slip boundary velocity. The others were involved with the generalization of the bounce-back rule by allowing the mix of bounce back and specular reflection (Succi 2002). These approaches involve complicated treatments at the boundary. Currently, Maxwell slip model is the most common approach to describe the slip velocity, in particular for rarified-gas-flow problems. In the Maxwell slip model, the slip velocity is a function of Knudsen number, gradient of velocity, and a so-called accommodation coefficient. The main disadvantage here is the high dependency of the slip velocity on the accommodation coefficient, which is a free parameter related to diffusive reflection. In most of the cases, a limited knowledge of this parameter led to significant deviation of the model results from the benchmark values (Maxwell 1879; Myong 2004; Kim et al. 2007; Chen and Tian 2009). Several attempts have been made to attribute a physical meaning to the accommodation coefficient by use of the Langmuir theory of equilibrium adsorption (Myong 2004; Myong et al. 2005). In these approaches, at large Knudsen numbers, the gas molecules interact with the solid surfaces by mean of fluid/solid adhesive forces; consequently, the gas molecules are allowed to adsorb at the surface and may desorb to the pore space after some time lag. This time lag causes macroscopic slip velocity at the solid surface. The lag is considered to be influenced by the adsorption; hence, it is a function of the amount of gas adsorbed at the surface, pressure, temperature, and some gas/solid physical properties that can be described by use of the equilibrium Langmuir isotherm. These approaches, being referred to as the Langmuir slip model, have been applied to several microflow problems successfully (Myong 2001, 2004; Myong et al. 2005).

Our previous numerical and experimental investigations on gas storage and transport have revealed the importance of wall-dominated transport in organic-rich shale (Fathi and Akkutlu 2012, 2009; Kang et al. 2011). On the basis of these investigations, the Knudsen flow in organic-rich shale can be considered a manifestation of several molecular-level transport phenomena at the large scale. In Kang et al. (2011), for example, the flow has been considered to develop by the kerogen pore walls as a result of slippage of the free gas molecules, and surface transport (or hopping) of the adsorbed molecules. Here, we propose to modify the existing LBM with a Langmuir slip boundary condition to incorporate into laminar flow both the slippage and the surface-transport mechanisms. In the new Langmuir slip model, called LBM-Ls, the surface transport of the adsorbed phase is introduced as a moving wall in the model organic pores. The wall velocity in this case is caused by the adsorbed-phase gradient and can be calculated locally at each timestep by use of the Langmuir-isotherm equation. The slippage, on the other hand, is considered a specular reflection of the fluid particles by the wall. We show application of the new model in simple pore geometry: an organic capillary. We show that the new Langmuir slip model recovers the analytical solution for Poiseuille flow in large nanotubes. Next, the sensitivity of flow is discussed in bundles of capillaries with smaller diameters, where Knudsen number is increased significantly. The results show molecular streaming effect by the walls on the overall gas transport in capillaries. In addition, under certain conditions, the parabolic fluid-velocity profile of the laminar flow appears and at different conditions the profile appears somewhat more uniform across each capillary indicating viscous decoupling and diffusive mass transport.

Lattice Boltzmann Model

LBM is developed to overcome some of the disadvantages of the lattice gas cellular automaton, such as the statistical noise and the appearance of extra terms in the upscaled Navier-Stokes equations. Fundamentally, in LBM, the discrete Boolean variables of the lattice gas cellular automaton describing the particle occupation are replaced by a particle-distribution function. This approach eliminates the statistical noise issue while keeping all the advantages of locality in the kinetic form of the lattice gas cellular automaton (Wang and Reed 2009). LBM is recognized with the lattice Boltzmann equation, lattice pattern, and local equilibrium distribution function. The lattice/Boltzmann equation is a combination of two processes: (1) streaming, in which each fluid particle moves in a direction of its velocity to the neighbor lattice node; and (2) collision, where particles arriving at a node collide and change their velocity direction according to collision operator Ω. The lattice Boltzmann equation can be written as

$$f_a(x_a + e_a\Delta t, t + \Delta t) = f_a(x_a, t) + \Omega(f_a)$$
$$a = 0, 1, \ldots, N, \quad \ldots\ldots\ldots\ldots (1)$$

where f_a is the distribution function of particles; x and t are lattice space and lattice time dimensions, respectively; Δt is incremental lattice timestep (ts); and e_a is the velocity vector of the particle at node a. Definition of the lattice pattern depends on the dimension of space we want to simulate; however, to recover the correct flow equations, it is necessary to use specific lattice patterns that provide sufficient lattice symmetry, such as square and hexagonal lattices (Frisch et al. 1986). In the LBM equation the number of possible particle positions and their velocity directions are limited to the number of nodes in each lattice. The number of velocity magnitudes, which distinguishes different lattice patterns, is also limited. More simplification of general lattice equation has been made by assuming uniform particle mass (mu) equal to unity that leads to equivalent microscopic velocities and momenta for the lattice. 2D simulations, a nine-speed square lattice (**Fig. 1;** left) called D2Q9 has been used extensively, where each particle moves one lattice unit (lu) at its velocity defined by e_a (Eq. 2) and in one of the eight directions indicated by 1 through 8 in Fig. 1 (left). On the basis of this nomenclature, a particle at Position 0 is called the rest particle and has a zero velocity.

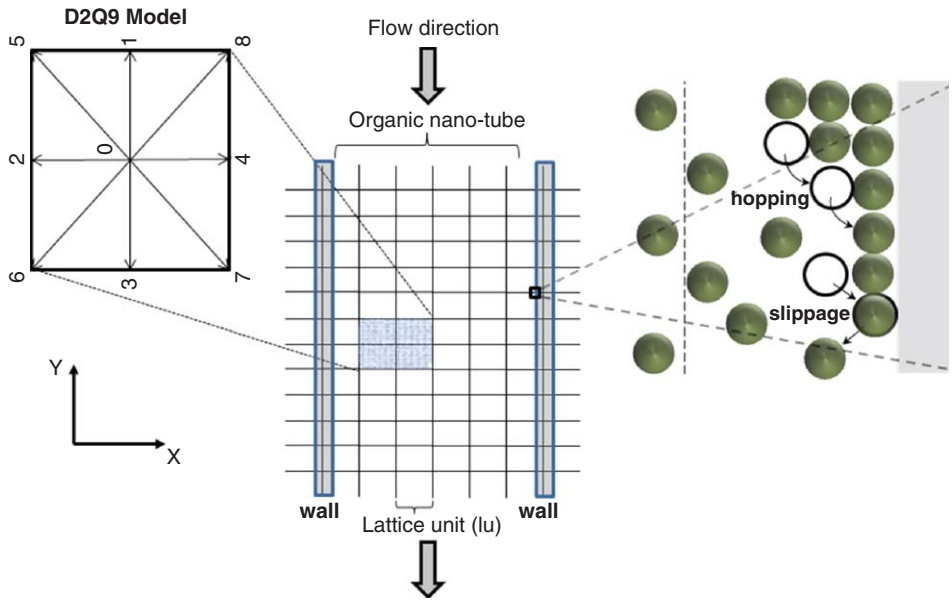

Fig. 1—(a) D2Q9 lattice pattern, (b) lattice geometry and velocity directions in the organic capillary, and (c) molecular transport mechanisms by the organic capillary wall.

$$e_a = \begin{cases} (0,0) & a = 0, \\ \left[\cos\frac{(a-1)\pi}{4}, \sin\frac{(a-1)\pi}{4}\right] & a = 1,2,3,4 \\ \sqrt{2}\left[\cos\frac{(a-1)\pi}{4}, \sin\frac{(a-1)\pi}{4}\right] & a = 5,6,7,8, \end{cases} \quad \ldots\ldots\ldots\ldots\ldots\ldots (2)$$

The next step is to define a proper collision operator. The Bhatnagar-Gross-Krook (BGK) collision operator with a single relaxation time is often used for the purpose. The BGK collision operator is derived on the basis of linearization of the collision operator around the equilibrium state, neglecting the higher-order terms, and assuming $\Omega_a(f^{eq})$ equal to zero. Hence, the BGK collision operator can be written as (Bhatnagar et al. 1954)

$$\Omega(f_a) = -\frac{f_a - f_a^{eq}}{\tau}. \quad \ldots\ldots\ldots\ldots\ldots\ldots\ldots\ldots (3)$$

Here, τ is the relaxation time that is assumed constant in the case of nearly incompressible fluids. This assumption introduces the second order truncation error in the lattice Boltzmann equation. In isothermal LBM models, this error is completely absorbed into the kinematic viscosity υ, defined in He et al. (1998) as

$$\upsilon = (\tau - 0.5)RT, \quad \ldots\ldots\ldots\ldots\ldots\ldots\ldots\ldots (4)$$

where R is the universal gas constant and T is the temperature. In the D2Q9 model, RT=1/3 is taken. Equation 4 defines the relation between relaxation time and kinematic viscosity in continuum flow, suggesting that flow is controlled by Reynolds number. However, in the case of transport in microchannels with large Knudsen number, the flow is controlled by Knudsen number. Therefore, the relaxation time needs to be corrected for the Knudsen-number value. In this study, we have used the approach introduced in Suga et al. (2010), where the effective relaxation time is a function of Knudsen number, as follows:

$$\tau^* = \tau\,\Psi(Kn) \quad \ldots\ldots\ldots\ldots\ldots\ldots\ldots\ldots (5)$$

The function $\Psi(Kn)$ was first developed by Stops (1970). Here, we use a simplified form of the function as introduced by Suga et al. (2010):

$$\Psi(Kn) = \frac{2}{\pi}\arctan\left(\sqrt{2}Kn^{-3/4}\right), \quad \ldots\ldots\ldots\ldots\ldots\ldots (6)$$

where Knudsen number can be found by use of

$$Kn = \frac{\upsilon}{H}\sqrt{\frac{\pi}{2RT}}. \quad \ldots\ldots\ldots\ldots\ldots\ldots\ldots\ldots (7)$$

Application of Eq. 5 introduces the wall effect more clearly and implies that some of the particles colliding with the wall have shorter effective relaxation time (τ*) than the case where the wall effect was ignored (i.e., by use of τ instead), which appears as a mean slip velocity at the wall at macroscopic level.

Having introduced the lattice Boltzmann equation and the lattice pattern, we need to define the local equilibrium distribution function $\int_a^{eq}$ faeq appearing in Eq. 3. This is a very important function that defines what type of flow equations are solved by use of the lattice Boltzmann equation. We are using the equilibrium distribution function derived by Qian et al. (1992) to solve the Navier-Stokes problems (i.e., Eq. 8); however, solving different sets of transport equations, one needs to derive the corresponding equilibrium distribution function by use of a general power series of macroscopic velocities (Zhou 2004),

$$\int_a^{eq} = \omega_a\rho\left[1 + \frac{3(e_a\cdot U)}{e^2} + \frac{9(e_a\cdot U)^2}{2e^4} - \frac{3(U\cdot U)}{2e^2}\right]. \quad \ldots\ldots (8)$$

Here, the weights ω_a are equal to ω_0=4/9, ω_1= ω_2= ω_3= ω_4= 1/9, and ω_5= ω_6= ω_7= ω_8 = 1/36 and e is lattice velocity defined as the lattice size Δx over the lattice timestep Δt. Fluid density ρ and velocity U are macroscopic quantities that can be obtained by use of the following fundamental expressions:

$$\rho = \sum_{a=0}^{8} f_a\,; \quad U = \frac{1}{\rho}\sum_{a=0}^{8} e_a f_a\,. \quad \ldots\ldots\ldots\ldots\ldots\ldots (9)$$

Langmuir Slip Boundary Condition

As stated earlier, the interactions between fluid/fluid and fluid/solid molecules can be incorporated into the LBM by use of appropriate boundary conditions. The Langmuir slip model has been developed, on the basis of the Langmuir theory, to overcome the commonly used Maxwell slip model disadvantage of having

the accommodation coefficient as a free parameter. In the Langmuir slip model, gas molecules are assumed to interact with the solid surface; they adsorb to the walls because of adhesive forces and then after some time lag, they are released to the fluid (i.e., desorb) (Myong 2004; Myong et al. 2006). The amount of adsorbed gas molecules at the solid surface follows the equilibrium Langmuir isotherm defined as

$$\alpha = \frac{C_\mu}{C_{\mu s}} = \frac{KC}{1+KC}, \quad \ldots\ldots\ldots\ldots\ldots\ldots\ldots (10)$$

where $C_{\mu s}$ is the maximum monolayer adsorption capacity, C_μ the adsorbed gas density, K the Langmuir partition coefficient, and C the free-gas density. By use of a proper equation of state (EOS) for the free gas, Eq. 10 can also be written in terms of pore pressure as

$$\alpha = \frac{V_a}{V_{a\max}} = \frac{\frac{1}{P_L}P}{1+\frac{1}{P_L}P}, \quad \ldots\ldots\ldots\ldots\ldots\ldots\ldots (11)$$

where $V_{a\max}$ is the maximum monolayer adsorbed gas volume, V_a the adsorbed gas volume, P_L the Langmuir pressure (i.e., pressure at which $V_a = V_{a\max}/2$), and P the pore pressure. α is at a fixed temperature and is a function of pressure P and of the gas and solid properties introduced by the Langmuir parameters. We now introduce the fluid velocity by the wall as a function of α, as follows:

$$U_W = (1-\alpha)U_{g,\text{slip}} + \alpha\, U_{\text{surf}}, \quad \ldots\ldots\ldots\ldots\ldots (12)$$

where U_{surf} is the local wall velocity caused by the adsorbed-phase transport (i.e., the surface transport) and $U_{g,\text{slip}}$ is the velocity of the gas one mean free path distance away from the wall. In this equation, as the free-gas pressure is increased, the amount of adsorbed gas eventually reaches the maximum volume for monolayer adsorption ($V_{a\max}$); in this limit, α becomes unity and the slip velocity reaches the wall velocity. On the other hand, as pore pressure drops, α decreases, and in the limit when the adsorbed gas amount becomes negligible, the slip velocity becomes equal to the fluid velocity.

To implement the Langmuir boundary condition, we follow the procedure presented by Chen and Tian (2009, 2010). In this approach, solid wall is overlapped with boundary Nodes 3-0-1, as shown in Fig. 1. Considering boundary Node 0 lying on left wall in Fig. 1 (middle), its distribution function needs to be evaluated by use of the Langmuir slip model. Following the Chapman-Enskog method, the distribution function at the wall can be divided into equilibrium and nonequilibrium parts, as follows (Chen and Doolen 1998):

$$f(0,t) = f^{\text{eq}}(0,t) + (1-\eta)f^{\text{neq}}(0,t), \quad \ldots\ldots\ldots\ldots (13)$$

where η is defined as $\eta = 1/(\tau_{\text{eff}} + 0.5)$ and superscripts eq and neq correspond to equilibrium and nonequilibrium parts of the distribution function, respectively. By use of the analogy to the Langmuir model, the equilibrium and nonequilibrium parts of the distribution function given in Eq. 13 can also be written as in Chen and Tian (2009, 2010):

$$\begin{cases} f^{\text{eq}}(0,t) = \alpha f^{\text{eq}}(W,t) + (1-\alpha)f^{\text{eq}}(g,t) \\ f^{\text{neq}}(0,t) = \alpha f^{\text{neq}}(W,t) + (1-\alpha)f^{\text{neq}}(g,t) \end{cases} \quad \ldots\ldots\ldots (14)$$

At any time t, the macroscopic quantities (e.g., fluid velocities and densities) of the flow are known at the nodes; thus, the equilibrium and nonequilibrium distribution functions can be determined freely. In this study, because of the adsorbed-phase transport, the wall is assumed to move with the local velocity of adsorbed phase. The latter is a function of local pore pressure and α. Here, the fluxes by the wall are defined assuming Fickian diffusive transport. Hence, the adsorbed and free mass fluxes are

$$\begin{aligned} J_{\text{ads}} &= U_{\text{surf}}\frac{\rho_{\text{ads}}}{M} = -D_S\frac{\partial C_\mu}{\partial x} \\ J_{\text{free}} &= U_{g,\text{slip}}\frac{\rho_g}{M} = -D_K\frac{\partial C}{\partial x} \end{aligned}, \quad \ldots\ldots\ldots\ldots\ldots (15)$$

respectively, where M is the molecular weight of the gas. Adsorbed-phase flux at the wall (J_{ads}) is a function of adsorbed-phase diffusion coefficient, or surface diffusion coefficient D_s, and the gradient of adsorbed-gas density. Knowing the velocity and density of the gas close to the wall (U_g, ρ_g) at each timestep we can find this gradient by use of the chain rule and the Langmuir isotherm (Eq. 10), as follows:

$$\frac{\partial C_\mu}{\partial x} = \frac{\partial C_\mu}{\partial C}\frac{\partial C}{\partial x} = \frac{KC_{\mu s}}{(1+KC)^2}. \quad \ldots\ldots\ldots\ldots\ldots (16)$$

Hence, with the use of Eqs. 15 and 16, the local wall velocity U_{surf}, becomes

$$U_{\text{surf}} = \left(\frac{D_S}{D_K\rho_{\text{ads}}}\right)\left[\rho_g\, U_{g,\text{slip}}\frac{KC_{\mu s}}{(1+KC)^2}\right]. \quad \ldots\ldots\ldots (17)$$

Knowing the wall temperature and velocity, at each timestep, the equilibrium distribution function at the wall can be found (Tang et al. 2005, 2008; Chen and Krafczyk 2009; Chen and Tian 2009, 2010):

$$f^{\text{eq}}(W,t) = f^{\text{eq}}(\rho_g, T_W, U_{\text{surf}}, t) + O(\varepsilon^2), \quad \ldots\ldots\ldots\ldots (18)$$

where the local fluid density at the wall is approximated with gas fluid density at the nearby cell. This introduces a second-order truncation error because ε is an arbitrary small quantity. The nonequilibrium distribution function at the wall can also be approximated as follows (Chen and Doolen 1998; Tang et al. 2005, 2008; Chen and Tian 2009, 2010):

$$\begin{cases} f^{\text{neq}}(W,t) = f^{\text{neq}}(\rho_g, T_g, U_{g,\text{slip}}, t) + O(\varepsilon^2) \\ f^{\text{neq}}(W,t) = f(\rho_g, T_g, U_{g,\text{slip}}, t) - f^{\text{eq}}(\rho_g, T_g, U_{g,\text{slip}}, t) + O(\varepsilon^2) \end{cases}. \quad \ldots\ldots\ldots\ldots\ldots (19)$$

Substituting the expressions of f^{eq} (Eq. 18) and f^{neq} (Eq. 19) into Eq. 14, the final form of the distribution function at the wall can be approximated as

$$\begin{aligned} f(0,t) = {} & \alpha f^{eq}(\rho_g, T_W, U_{\text{surf}}, t) + (1-\alpha)f^{eq}(\rho_g, T_g, U_{g,\text{slip}}, t) \\ & + (1-\eta)\left[f(\rho_g, T_g, U_{g,\text{slip}}, t) - f^{eq}(\rho_g, T_g, U_{g,\text{slip}}, t)\right] + O(\varepsilon^2) \end{aligned} \quad \ldots\ldots\ldots\ldots\ldots (20)$$

Application of this method introduces second-order accuracy; therefore, both stability and precision are preserved by use of this approach (Chen and Tian 2010).

Adsorptive and Cohesive Forces

To describe the interaction forces between fluid molecules and walls during LBM simulation, we use Eq. 21, which was introduced earlier by Sukop and Or (2004):

$$F_{\text{ads}}(x,t) = -G_{\text{ads}}\Psi(x,t)\sum_{a=0}^{8}\omega_a s(x+e_a)e_a, \quad \ldots\ldots\ldots (21)$$

where Ψ is interaction potential function, G_{ads} is the interaction strength (that is positive for nonwetting fluid and negative for wetting fluid), ω_a is a weighting factor as defined earlier in Eq. 8, and s is an index function equal to unity if the site at $x+e_a$ is a solid and equal to zero otherwise. Interaction potential function Ψ can be defined as amonotonically increasing and bounded function (Shan and Chen 1993). Here, we use a simple form of exponential function where Ψ is a function of fluid density and a constant ρ_0 (Shan and Chen 1993; Sukop and Thorne 2006),

$$\Psi(\rho) = \rho_0\left[1 - \exp\left(\frac{-\rho(x,t)}{\rho_0}\right)\right]. \quad \ldots\ldots\ldots\ldots (22)$$

To simulate the two-phase transport of free and adsorbed gas molecules, we also need to include long-range forces between the

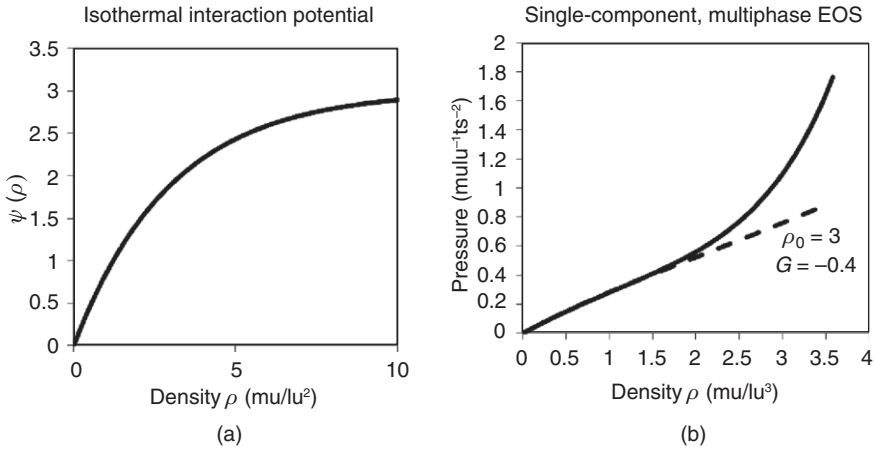

Fig. 2—Interaction potential function changes with density (a), and history matching of the methane pressure/density curve (b).

free and adsorbed gas molecules. However, for simplicity, we consider only the cohesive forces between adsorbed molecules at the wall and their neighbors in the fluid by use of the formulation introduced earlier by Shan and Chen (1993):

$$F(x,t) = -G\,\Psi(x,t)\sum_{a=0}^{8}\omega_a\Psi(x+e_a\Delta t,t)e_a. \quad \ldots\ldots\ldots (23)$$

Here, G is the interaction strength, which is negative for attractive forces and becomes more pronounced as the density of the adsorbed layer increases. Introduction of the interaction forces between the particles in the LBM formulation leads to a nonideal EOS (Eq. 24) that can be used to simulate the interface dynamics between the liquid and gas phases (He and Doolen 2002; Sukop and Thorne 2006):

$$P = \rho RT + \frac{GRT}{2}[\Psi(\rho)]^2. \quad \ldots\ldots\ldots\ldots\ldots\ldots (24)$$

Fig. 2 illustrates the interaction potential as a function of density on the left and presents a pure-methane pressure/density diagram on the right, both at 293.15 K. The coefficient ρ_0 and the interaction strength G are estimated to be equal to 3 and −0.4, respectively, by matching the pressure/density diagram of methane by use of Eqs. 22 and 24. Similar investigations should be made when other types of gases or gas mixtures are considered for simulation.

In the following, we are solving the Boltzmann equation (Eq. 1) by use of the velocity and collision operator defined in Eqs. 2 and 3, where we use the equilibrium distribution function presented in Eq. 8. We also apply the Knudsen-number correction (Eq. 5) to account for the Knudsen number-controlled flow regime. For the boundary conditions at the inlet and outlet, we use periodic boundary conditions where the capillary acts as a closed system. The modified Langmuir slip boundary condition as defined in Eqs. 10 through 20 is applied to account for both adsorbed-phase transport and slippage by the walls. The body forces (cohesive and adsorptive forces introduced by Eqs. 21 and 23) are added through a directionally dependent force term in the equilibrium distribution that partially redistributes the particle motion at a node in the direction of the force term.

Simulation Results and Discussions

For numerical simulation purpose, first we choose a simple 2D capillary where the gas transport is confined between two parallel walls (Fig. 1). Initially, the capillary has width L_x=100 nm (or 50 lu) and length L_y=200 nm (or 100 lu), although the width plays an important role in our analysis; hence, later it will be changed significantly as part of a sensitivity analysis. The flow is from top to the bottom. Fig. 1 shows on the right the adsorbed- and free-gas transport mechanisms contributing to the total mass flux by the walls. The adsorbed-phase transport is driven by the adsorbed-phase gradient where the adsorbed molecules can overcome the local interactions with the wall and develop a hopping mechanism by the wall. The pressure difference between the inlet and outlet also causes the free gas molecules to be transported as free gas phase inside the tube and, at high Knudsen number, to slip right by the wall.

In all the numerical simulations, the system temperature is fixed to the ambient temperature of 298.15 K and flow of pure methane is assumed at 1,623 psi at time equal to zero. Average adsorbed-gas density ρ_{ads}, Langmuir pressure P_L, and volume $V_{a\max}$ are 0.4 g/cm^3, 1,800 psi, and 0.1962 cm^3, respectively, borrowed from our previous experimental work presented in Kang et al. (2011). These values correspond to methane adsorption in organic (kerogen) pores of shale samples. Periodic boundary condition is applied at the capillary inlet and outlet. We assume density and temperature variations are small across the tube so that the Kn remains nearly constant across the capillary. In this study, LBM is initially used applying two different boundary conditions. The first one is the commonly used bounce-back boundary condition at the walls where the fluid particle bounces back to the fluid node opposite to its incoming direction (Succi 2001). The other boundary condition is the newly developed Langmuir slip boundary condition of the LBM-Ls as introduced in the preceding section.

Fig. 3 shows the velocity profile of methane transport in a 100-nm capillary. During the simulation, the Knudsen number is small and equal to 5.6×10^{-3}; thus, the continuum-flow regime prevails. Fig. 3 is generated to compare and validate the numerical results of LBM simulations by use of the analytical solution of Poiseuille flow. Indeed, the numerical results show a reasonable match with the analytical solution. Fig. 3 also shows that the fluid velocity at the wall is zero; thus, the fluid dynamics is not sensitive to the slip and to the amount of adsorbed phase and its surface transport, during the continuum-flow regime. These solutions are our basis for the rest of our analysis where we investigate the capillary-width and transport-mechanism effects on the gas dynamics.

Next, sensitivity to the capillary size is investigated by use of LBM-Ls to simulate gas dynamics in a bundle of capillaries. For the purpose, we divide the 100-nm ($L_{x,1}$) model capillary used earlier in Fig. 3 to a bundle of five 20-nm ($L_{x,2}$)-wide capillaries. **Fig. 4a** shows the computed velocity distributions with color indices on the left and the cross-sectional velocity profiles across the bundle on the right. On the basis of Poiseuille's law, one would expect the following relationship should hold between average velocity in 20 ($\overline{U}_{y,2}$) and 100 ($\overline{U}_{y,1}$) nm capillary tubes: $\overline{U}_{y,2} = \overline{U}y,1(L^2_{x,2}/L^2_{x,1})$. Here, the capillary-width square ratio of the two organic capillary bundles is also equivalent to their permeability ratio. The predicted velocity of the fluid in the 100-nm tube changes between zero and 1.6×10^{-6} lu/ts across the half-length of the capillary. (The negative sign indicates that the flow is downward.) So, if an average velocity value of 0.8×10^{-6} lu/ts is

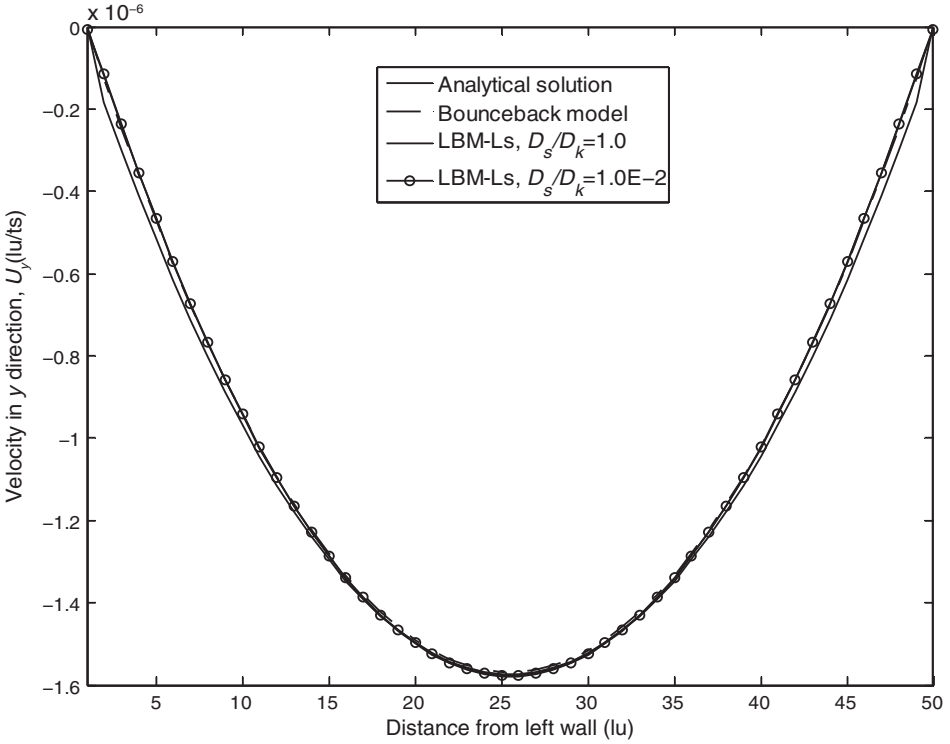

Fig. 3—Comparison of numerical solution of gas flow in organic capillary by use of bounce-back and Langmuir slip model and analytical solution. Kn=5.6×10^{-3}, Re=3.4×10^{-5}, and ν=0.13 lu^2/ts.

taken for that pore, then, once the capillary size is reduced to 20 nm, one would expect the average velocity in the smaller capillary to be equal to $(0.8\times10^{-6})(20)^2/(100)^2 = 3.2\times10^{-8}$ lu/ts. Fig. 4a shows that LBM-Ls agrees reasonably well with this value, indicating that a reduction in organic capillary width leads to a reduction in permeability and fluid velocity, in accordance with the classical theory. Note, however that during the simulations the boundary effects are limited: the capillary width is still large enough; hence, the Knudsen number is small (Kn<0.028) and therefore no measurable effect of slip is recorded; and D_S/D_K is taken as small, indicating that the surface transport of the adsorbed phase is kept negligible during the simulation. Consequently, the parabolic velocity profile is preserved, indicating that convective gas transport is dominant in the bundle.

In Fig. 4b, the simulation results are shown when the surface transport is kept dominant by increasing the ratio of diffusion coefficients by two orders of magnitude. Note that this is not an uncommon situation in organic nanotubes; as discussed in Kang et al. (2011), the adsorbed-phase transport can dominate the gas transport. It is clear that the surface transport of the adsorbed methane molecules makes the velocity right at the walls nonzero (1.24×10^{-7} lu/ts) and, more importantly, influences the whole velocity profile across the capillaries significantly. Now the surface transport leads to one order of magnitude larger average velocity: 3.5×10^{-7} lu/ts.

In **Fig. 5,** the Knudsen number is increased to 0.056 by simply doubling the number of capillaries in the bundle. Hence, we have ten 10-nm-wide capillaries in the bundle now. In this case, the predicted gas velocity is distributed somewhat uniformly at the center of the capillaries because the parabolic velocity profiles no longer develop across the capillaries. Hence, the transport mechanism is not convective in this bundle but diffusive in nature. Note that the velocity is increased by nearly a factor of four when the sizes of the capillaries are reduced by half. In addition, even though surface transport is not changed, the kinetic effects are more dominant. The transport by the walls is now caused by both surface transport and slip. The effective velocities across the capillaries are now two orders of magnitude larger than 1.6×10^{-8} lu/ts, which is the value one would have predicted by use of classical theory. Interestingly, when D_S/D_K =3, we observe that the fluid velocity by the walls becomes larger than the velocity of the fluid at the center. These results are important and point to the existence of molecular streaming by the walls and its influence on the gas transport. The predicted velocities in 10-nm size capillaries are comparable with those velocities earlier computed for gas in the 100-nm capillary. Molecular streaming because of surface transport and slip indeed enhances the gas transport in the organic nanopores. The surface transport effect appears in the figures as nonzero velocity at the walls, where location across capillary is exactly equal to zero or 50 lattice units. The slip, on the other hand, develops inside the capillary tube right by the walls; it appears as a jump in the velocity profile, when it exists. Accordingly, at the first sight, one would argue that D_S/D_K should always be small; hence, the main contribution to the enhancement in gas transport must be caused purely by slippage. This statement, however, needs to be revisited with the next sensitivity analysis by use of LBM-Ls.

Fig. 6 shows the importance of the surface transport mechanism on the overall gas transport in the organic capillaries. Obviously, the surface transport of the adsorbed phase is negligible at large capillaries with a size on the order of 100 nm. It becomes somewhat influential on the transport when the capillary size is on the order of 10 nm. Notice in Fig. 6 the straight line with a nonzero slope. The slope indicates the contribution of the surface transport, whereas the intercept indicates the contribution of the gas slippage. It is anticipated that the surface transport effect is dominant in micropores with sizes on the order of 1 nm. As with any LBM, LBM-Ls fails to accurately simulate the molecular dynamics at that scale.

The computed velocity vectors for varying combinations of controlling parameters are given in **Fig. 7.** At the top, we compare the change in velocity vectors across the capillary for varying Knudsen numbers, whereas D_s/D_k ratio is small. This clearly shows that the velocity magnitudes are larger in all the locations across the capillary for higher Knudsen number. Introducing more adsorbed phase transport by increasing the D_s/D_k ratio leads to higher velocities across the capillary in Fig. 7 (bottom).

In LBM-Ls, the velocity of the molecular streaming (i.e., U_W) is a function of α (i.e., the relative coverage of solid surface by

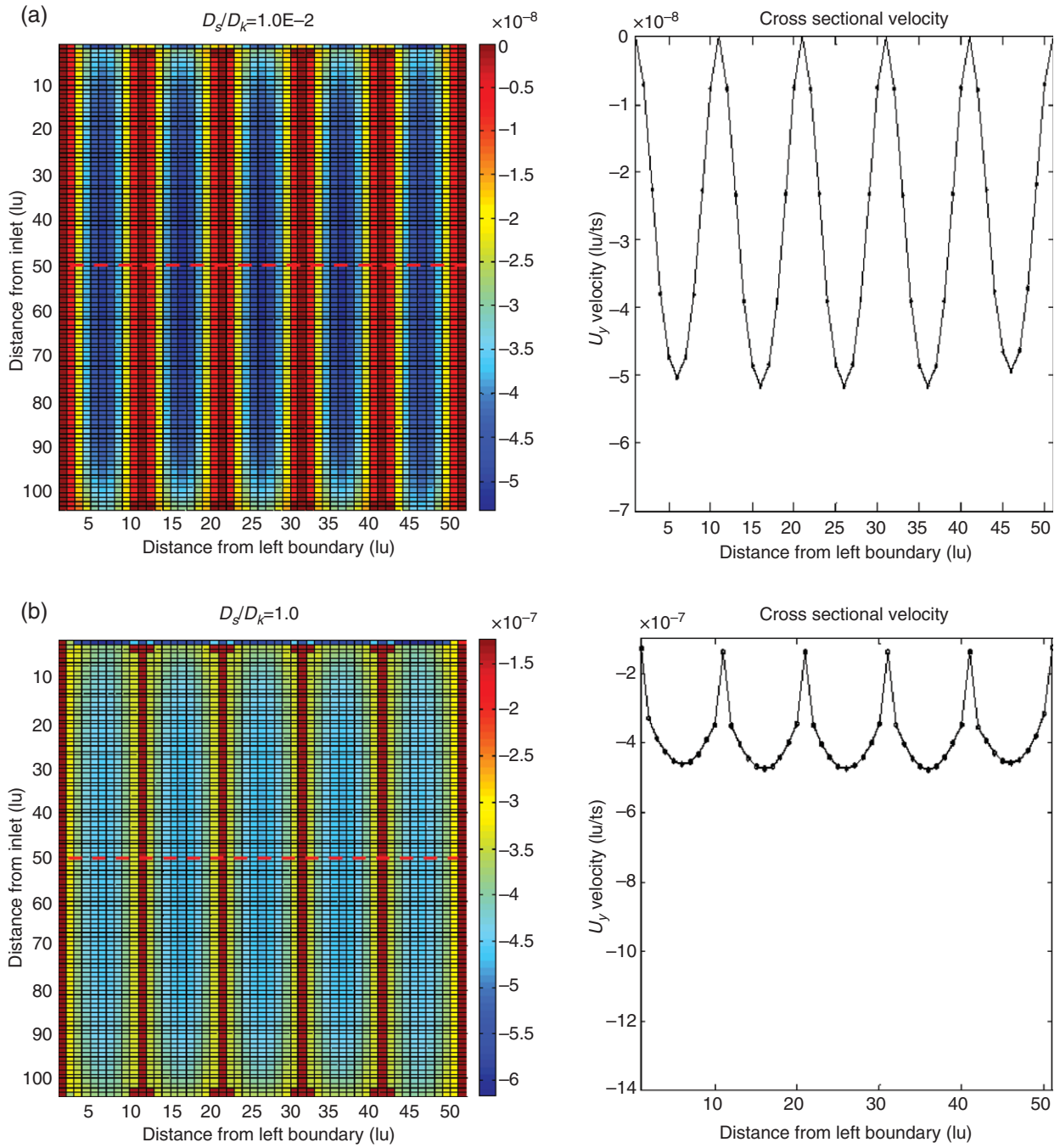

Fig. 4—Comparison of velocity distributions (a) and the cross-sectional velocity profiles (b) for a bundle of five organic capillaries with size 20 ×200 nm by use of LBM-Ls. D_S/D_K is taken equal to 0.01 (a) and 1.0 (b). Kn=0.028, Re=4.9×10^{-6}, and ν=0.65 lu^2/ts during the simulations.

the adsorbed gas molecules with respect to maximum monolayer adsorption capacity of the solid surface). To investigate the sensitivity of velocity profiles to α, **Fig. 8** depicts the change in velocity profiles with the maximum monolayer adsorption capacity $V_{a\max}$. Here, high Knudsen number (Kn=0.1) is considered such that both molecular transport mechanisms are active by the wall. The ratio of the diffusion coefficients is kept constant and equal to 1.0. As the maximum adsorption capacity $V_{a\max}$ is increased, because the internal surface area of the capillary is not changed, the amount of adsorbed phase increases too. This leads to a retardation effect and a preserved parabolic profile on the velocity. It is also interesting that the slip velocity at the wall decreases as the capacity is increased because an increasing portion of the solid surface area is now covered with adsorbed gas; consequently, the adsorbed layer becomes somewhat more homogeneous. In this case, the adsorbed-phase gradient becomes smaller, retarding the adsorbed-phase transport. Similar behavior has been reported earlier by use of a semianalytical approach to fluid flow in tight formations by Fathi and Akkutlu (2009). They showed that increasing the amount of adsorbed gas retards the overall gas transport in tight formations. In Do (1998), it is also mentioned that the adsorbed-phase transport is directly related to the heterogeneity in the adsorption layer.

Here, we would like to open a parenthesis to discuss the simulation results by use of the bounce-back condition. Our results have shown that, even though the bounce-back condition results in no-slip velocity at the wall within the continuum limit (Myong 2001), at higher Knudsen numbers nonzero slip velocity develops at the wall as a result of the kinetic nature of the lattice Boltzmann equation. Unlike the previous cases performed at high pressure, here we discuss the simulation results at low pressure where the adsorption effect is negligible. **Fig. 9** shows the numerical

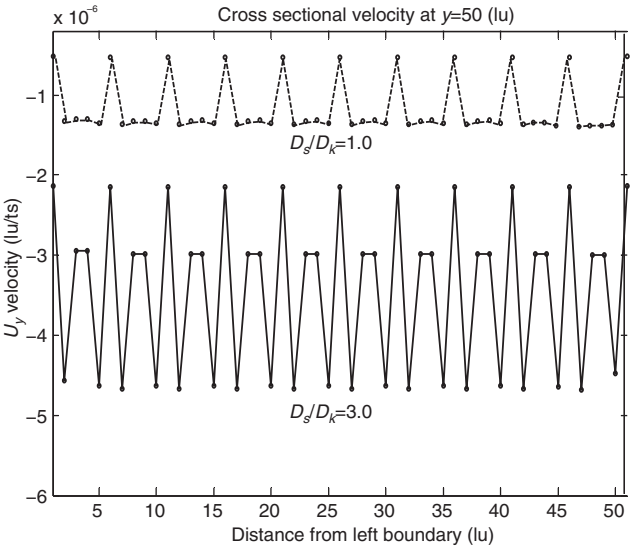

Fig. 5—Comparison of two cross sectional velocity profiles for a bundle of ten organic capillaries with size 10 ×200 nm by use of LBM-Ls at two separate diffusion coefficient ratio values. Kn=5.6×10^{-2}, Re=3.4×10^{-6}, and ν=1.29 lu^2/ts during the simulations.

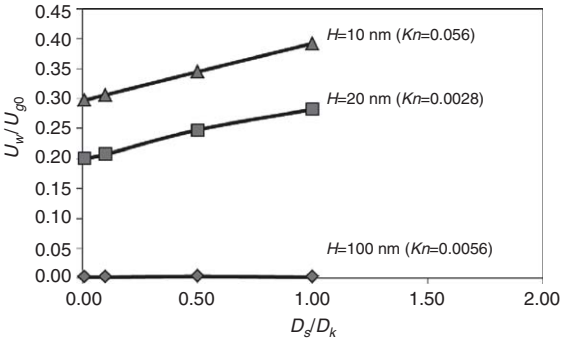

Fig. 6—Surface diffusion effect on molecular streaming velocity. U_W of gas in organic capillary with varying sizes. The velocity is normalized with the velocity of free gas at the center of the capillary, U_{g0}. Surface diffusion coefficient D_S is normalized with the diffusion coefficient of the bulk gas, D_K.

velocity profiles across the 100- and 20-nm capillaries at 100-psi average pressure. The figure also includes the analytical solution corresponding to flow in a 100-nm capillary, as the solid line, for comparison.

Clearly, with the decreasing capillary size, the parabolic velocity profile is transformed into a uniform plug-like velocity profile at the central portion of the capillary. Furthermore, the estimated velocities by the wall are nonzero, suggesting that the flow experiences gas slippage. Interestingly, the estimated velocities near the wall are significantly higher than that at the center of the 20-nm capillary and the higher velocity values can be observed not only by the wall, but also deep into the capillary. Hence, the fluid flow behavior in a 20-nm capillary is fundamentally different from that in a 100-nm (or larger) capillary. For more details on numerical and experimental studies at low pressures and multiscale effects see Akkutlu and Fathi (2011) and Fathi et al. (2012).

Similar observations have previously been reported by King (2007) and Nie et al. (2002). On the basis of the kinetic theory of gases, dilute gas consisting of hard particles moving with high velocity and having elastic collisions is assumed. Knowing the position vector and momentum of each particle at some instant in time clearly, together with classical mechanics, would allow exact prediction of all future states of the system (Sukop and Thorne Jr. 2006).

Conclusions

In this study, a new lattice Boltzmann model (LBM-Ls) is proposed to include the pore-wall effects of small organic capillaries. In the model, the adsorbed-phase transport is introduced as a wall movement, the speed of which is calculated at each timestep on the basis of local pressure and its gradient. The numerical results are validated with the analytical solution of Poiseuille flow in the continuum flow limit. Next, the effects of actual pore size and adsorbed-phase transport are investigated. It is found that as the capillaries shrink to the order of nanometers, and hence the Knudsen number is increased, the transport mechanism is not convection anymore but diffusion under the influence of molecular streaming. In the future, the LBM-Ls will be applied to 3D kerogen pore-network models where tortuosity and permeability of the model porous media will be predicted. In addition, a new generation of LBM-Ls will be developed considering multiple phases in the presence of longer-range interactions to investigate the capillary condensation phenomenon.

Nomenclature

a = lattice node
C = free-gas concentration
C_μ = adsorbed-gas concentration
$C_{\mu s}$ = maximum adsorption capacity
D_k = tortuosity-corrected coefficient of molecular diffusion
D_s = surface diffusion coefficient
e = lattice velocity
f = distribution function
F = force
f^{eq} = equilibrium distribution function
G = interaction strength
H = diameter of capillary
J_{ads} = adsorbed-gas flux
J_{free} = free-gas flux
K = equilibrium partition (or distribution) coefficient
Kn = Knudsen number
L = capillary length
M = gas molecular weight
Re = Reynolds number
P = pressure
P_L = Langmuir pressure
R = universal gas constant
t = time
T = temperature
U = macroscopic velocity vector
$U_{g,\mathrm{slip}}$ = slip velocity
U_{surf} = adsorb phase velocity
U_W = wall velocity
V_a = adsorbed-gas volume
$V_{a\max}$ = maximum monolayer adsorbed-gas volume
x = lattice space
λ = gas molecules mean free path
μ = gas dynamic viscosity
ρ_g = gas density
ρ_{ads} = adsorbed-phase density
τ = relaxation time
τ^* = effective relaxation time
υ = gas kinematic viscosity
ω = weighting factor
Ω = collision operator
Ψ = potential function

Subscripts and Superscripts

ads = adsortptive
eq = equilibrium
g = gas
neq = nonequilibrium
W = wall

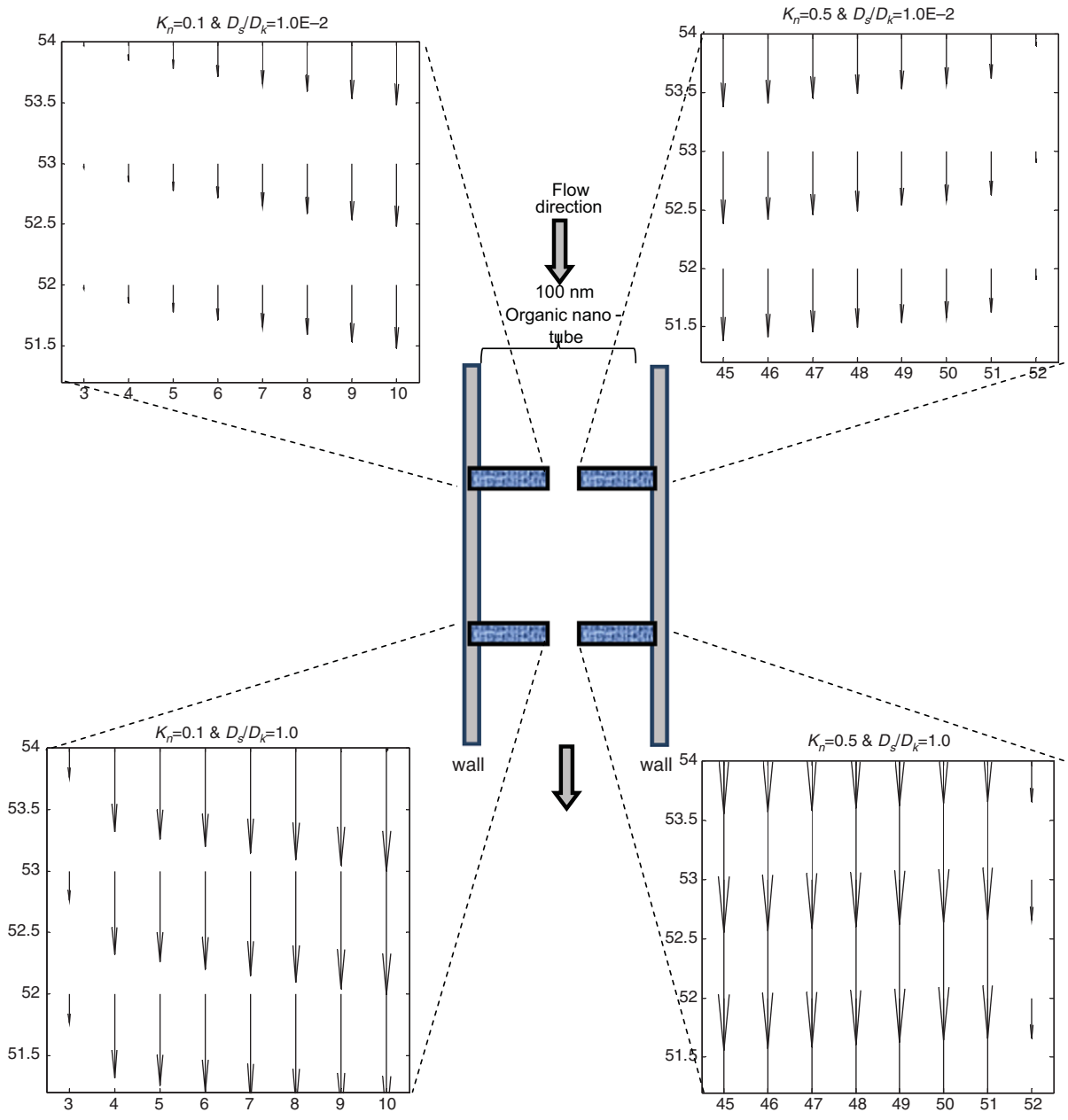

Fig. 7—Distribution of *y*-direction velocity vector along the nanotube wall as a function of Knudsen number and diffusivity ratio.

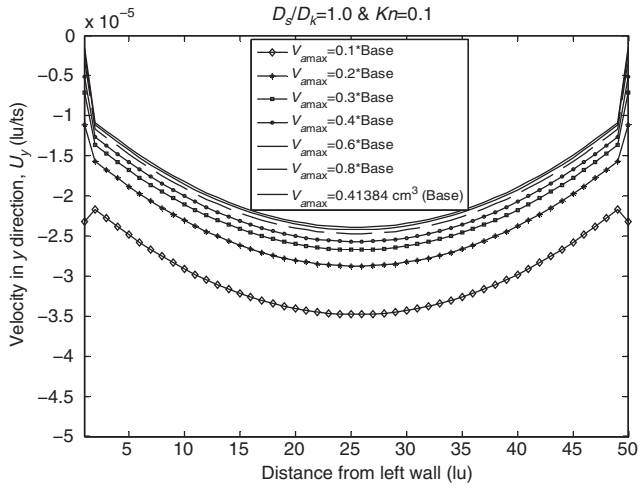

Fig. 8—Effect of maximum adsorption capacity on the gas velocity profile across the organic capillary by use of LBM-Ls.

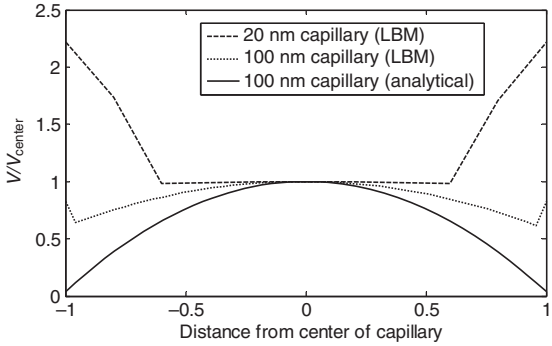

Fig. 9—Steady-state flow velocity profiles in capillaries with varying diameter at 100-psi average pressure. LBM simulation results include nonparabolic velocity profiles in small pores at low pressures. The velocity is somewhat more uniform (plug-like) at the center of the capillary. For all the capillaries, there exists significant slippage by the walls. For capillaries with a diameter less than 100 nm, the fluid velocity by the walls is larger than that at the center of the capillary. The wall effect is clearer in the case of a 20-nm pore.

Acknowledgments

The authors thank Devon Energy for the financial support provided for this work.

References

Akkutlu, I.Y., and Fathi, E. 2011. Multi-Scale Gas Transport in Shales with Local Kerogen Heterogeneities. Paper SPE 146422 presented during the SPE Annual Technical Conference and Exhibition held in Denver, Colorado, 30 October–2 November. http://dx.doi.org/10.2118/146422-MS.

Adesida, A., Akkutlu, I.Y., Resasco, D.E., et al. 2011. Characterization of Barnett Shale Pore Size Distribution using DFT Analysis and Monte Carlo Simulations. Paper SPE 147397 presented during the SPE Annual Technical Conference and Exhibition held in Denver, Colorado, 30 October–2 November. http://dx.doi.org/10.2118/147397-MS.

Ambrose, R.J., Hartman, R.C., Diaz-Campos, M., et al. 2012. Shale Gas In-Place Calculations Part I – New Pore-Scale Considerations. *SPE J.* **17** (1): 219–229. SPE-131772-PA. http://dx.doi.org/10.2118/131772-PA.

Bhatnagar, P.L., Gross, E.P. and Krook, M. 1954. A Model for Collision Processes in Gases. I. Small Amplitude Processes in Charged and Neutral One-Component Systems. *Phys. Rev.* **94** (3): 511–525. http://dx.doi.org/10.1103/PhysRev.94.511.

Chen, S., and Doolen, G.D. 1998. Lattice Boltzmann Method for Fluid Flows. *Annu. Rev Fluid Mech.* **30:** 329–364. http://dx.doi.org/10.1146/annurev.fluid.30.1.329.

Chen, S., and Krafczyk, M. 2009. Entropy Generation in Turbulent Natural Convection due to Internal Heat Generation. *Int. J. Therm. Sci.* **48:** 1978–1987. http://dx.doi.org/10.1016/j.ijthermalsci.2009.02.012.

Chen, S., and Tian, Z. 2009. Simulation of Microchannel Flow Using the Lattice Boltzmann Method. *Physica A* **388:** 4803–4810. http://dx.doi.org/10.1016/j.physa.2009.08.015.

Chen, S., and Tian, Z. 2010. Simulation of Thermal Micro-Flow Using Lattice Boltzmann Method with Langmuir Slip Model. *Int. J. Heat Fluid Flow* **31:** 227–235. http://dx.doi.org/10.1016/j.ijheatfluidflow.2009.12.006.

Dardis, O., and McCloskey, J. 1998. Lattice Boltzmann Scheme with Real Numbered Solid Density for the Simulation of Flow in Porous Media. *Phys. Rev. E.* **57** (4): 4834–4837. http://dx.doi.org/10.1103/PhysRevE.57.4834.

Diaz-Campos, M. 2010. Uncertainties in Shale Gas In-Place Calculations: Molecular Simulation Approach. MS thesis, University of Oklahoma, Norman, Oklahoma (April 2010).

Do, D.D. 1998. *Adsorption Analysis: Equilibria and Kinetics.* London, UK: Imperial College Press.

Fathi, E. and Akkutlu, I.Y. 2009. Matrix Heterogeneity Effects on Gas Transport and Adsorption in Coalbed and Shale Gas Reservoirs. *Transp. Porous Med.* **80:** 281–3044.

Fathi, E. and Akkutlu, I.Y. 2012. Mass Transport of Adsorbed-Phase in Stochastic Porous Medium with Fluctuating Porosity Field and Nonlinear Gas Adsorption Kinetics. *J. Transp. Porous Med.* **91** (1): 5–33. http://dx.doi.org/10.1007/s11242-011-9830-x.

Fathi, E., Tinni, A., and Akkutlu, I.Y. 2012. Shale Gas Correction to Klinkenberg Slip Theory. Paper SPE 154977 presented at the SPE Americas Unconventional Resources Conference held in Pittsburgh, Pennsylvania, 5–7 June. http://dx.doi.org/10.2118/154977-MS.

Frisch, U., Hasslacher, B., and Pomeau, Y. 1986. Lattice-Gas Automata for the Navier-Stokes Equation. *Phys Rev. Lett.* **56:** 1505–1508. http://dx.doi.org/10.1103/PhysRevLett.56.1505.

Guo, Z. L., Zhao, T. S., and Shi, Y. 2007. Discrete Effects on Boundary Conditions for the Lattice Boltzmann Equation in Simulating Microscale Gas Flows. *Phys. Rev. E* **76:** 056704. http://dx.doi.org/10.1103/PhysRevE.76.056704.

He, X. Y., Chen, S.Y., and Doolen, G.D. 1998. A Novel Thermal Model for the Lattice Boltzmann Method in Incompressible Limit. *J. Comput. Phys.* **146:** 282–300. http://dx.doi.org/10.1006/jcph.1998.6057.

He, X., and Doolen, G.D. 2002. Thermodynamic Foundations of Kinetic Theory and Lattice Boltzmann Models for Multiphase Flows. *J Stat. Phys.* **107:** 309–328. http://dx.doi.org/10.1023/A:1014527108336.

He, X., and Luo, L.S. 1997. A Priori Derivation of the Lattice Boltzmann Equation. *Phys. Rev. E.* **55:** 6333–6336. http://dx.doi.org/10.1103/PhysRevE.55.R6333.

Ho, C.M., and Tai, Y.C. 1998. Micro-Electro-Mechanical-Systems (MEMS) and Fluid Flows. *Annu. Rev. Fluid Mech.* **30:** 579–612. http://dx.doi.org/10.1146/annurev.fluid.30.1.579.

Kang, S.M., Fathi, E., Ambrose, R.J., et al. 2011. Carbon Dioxide Storage Capacity of Organic-Rich Shales. *SPE J.* **16**(4): 842–855. SPE-134583-PA. http://dx.doi.org/10.2118/134583-PA.

Kim, H., Kim, D., Kim, W., et al. 2007. Langmuir Slip Model for air Bearing Simulation Using the Lattice Boltzmann Method. *IEEE Trans. Magn.* **43:** 2244–2246. http://dx.doi.org/10.1109/TMAG.2007.893640.

King, M.R. 2007. Oscillatory Gas Flow in a Circular Nanotube. *The Open Nanoscience Journal.* **1** (1): 1874–1401. http://dx.doi.org/10.2174/1874140100701010001.

Loucks, R. G., Reed, R. M., Ruppel, S. C., et al. 2009. Morphology, Genesis, and Distribution of Nanometer-Scale Pores in Siliceous Mudstones of the Mississippian Barnett Shale. *J. Sedimentary Res.* **79:** 848–861. http://dx.doi.org/10.2110/jsr.2009.092.

Martys, N. S., and Chen, H. 1996. Simulation of Multicomponent Fluids in Complex Three-Dimensional Geometries by the Lattice Boltzmann Method. *Phys Rev E* **53:** 743–750. http://dx.doi.org/10.1103/PhysRevE.53.743.

Maxwell, J. C. 1879. On Stresses in Rarefied Gases Arising From Inequalities of Temperature. *Philos. Trans. R. Soc. London* **170:** 231–256. http://dx.doi.org/10.1098/rstl.1879.0067.

Myong, R.S. 2004. A Generalized Hydrodynamic Computational Model for Rarefied and Microscale Diatomic Gas Flows. *J. Comp. Phys.* **195:** 655–676. http://dx.doi.org/10.1016/j.jcp.2003.10.015.

Myong, R.S., Reese, J.M., Barber, R.W., et al. 2005. Velocity Slip in Microscale Cylindrical Couette Flow: The Langmuir Model. *Phys. Fluids* **17:** 087105. http://dx.doi.org/10.1063/1.2003154.

Myong, R.S., Lockerby, D.A., and Reese, J.M. 2006. The Effect of Gaseous Slip on Microscale Heat Transfer: An Extended Graetz Problem. *Int. J. Heat Mass Transfer* **49:** 2502–2513. http://dx.doi.org/10.1016/j.ijheatmasstransfer.2005.11.035.

Myong, R.S. 2001. Velocity-Slip Effect in Low-Speed Microscale Gas Flows. AIAA Paper No. 2001-3076.

Nie, X. B., Doolen, G. D., and Chen, S. Y. 2002. Lattice-Boltzmann Simulations of Fluid Flows in MEMS. *J. Stat. Phys.* **107:** 279–289. http://dx.doi.org/10.1023/A:1014523007427.

Or, D. and Tuller, M. 2002. The Role of Cavitation in Porous Media Desaturation Under Tension. *Wat. Resources Res* **38** (5): 19. http://dx.doi.org/10.1029/2001WR000282.

Qian, Y.H., d'Humieres, D., and Lallemand, P. 1992. Lattice BGK Models for Navier-Stokes Equation. *Europhys Lett.* **17:** 479–484. http://dx.doi.org/10.1209/0295-5075/17/6/001.

Ramstad, T., Oren, P., and Bakke, S. 2010. Simulation of Two-Phase Flow in Reservoir Rocks Using a Lattice Boltzmann Method. *SPE J.* **15** (4): 923–933. http://dx.doi.org/10.2118/124617-PA.

Roy, S., Raju, R., Chuang, H.F., et al. 2003. Modeling Gas Flow Through Microchannels and Nanopores. *J. Appl. Phys.*, **93** (8): 4870–4879. http://dx.doi.org/10.1063/1.1559936.

Shan, X., and Chen, H. 1993. Lattice Boltzmann Model for Simulating Flows With Multiple Phases and Components. *Phys. Rev. E* **47:** 1815–1819. http://dx.doi.org/10.1103/PhysRevE.47.1815.

Sondergeld, C.H., Ambrose, R.J., Rai, C.S. et al. 2010. Micro-Structural Studies of Gas Shales, Paper SPE 131771 presented at the SPE Unconventional Gas Conference, Pittsburg, Pennsylvania, 23–25 February. http://dx.doi.org/10.2118/131771-MS.

Stops, D. W. 1970. The Mean Free Path of Gas Molecules in the Transition Régime. *J. Phys. D: Appl. Phys.* **3:** 685–696. http://dx.doi.org/10.1088/0022-3727/3/5/307.

Succi, S. 2001. *The Lattice Boltzmann Equation for Fluid Dynamics and Beyond.* Oxford: Oxford University Press.

Succi, S. 2002. Mesoscopic Modeling of Slip Motion at Fluidsolid Interfaces With Heterogeneous Catalysis. *Phys. Rev. Lett.* **89:** 064502. http://dx.doi.org/10.1103/PhysRevLett.89.064502.

Suga, K., Takenaka, S., Ito, T., et al. 2010. Evaluation of a Lattice Boltzmann Method in a Complex Nanoflow. *Phys. Rev. E* **82:** 016701–016710. http://dx.doi.org/10.1103/PhysRevE.82.016701.

Sukop, M.C. and Or, D. 2004. Lattice Boltzmann Method for Modeling Liquid-Vapor Interface Configurations in Porous Media. *Water Resources Res.* **40:** W01509. http://dx.doi.org/doi:10.1029/2003WR002333.

Sukop, M.C., and Or, D. 2005. Lattice Boltzmann Method for Homogeneous and Heterogeneous Cavitation. *Phys Rev E* **71:** 046703–046711. http://dx.doi.org/10.1103/PhysRevE.71.046703.

Sukop, M.C. and Thorne Jr., D.T. 2006. *Lattice Boltzmann Modeling: An Introduction for Geoscientists and Engineers*. New York: Springer.

Tang, G.H., Gu, X.J., Barber, R.W., et al. 2008. Lattice Boltzmann Simulation of Nonequilibrium Effects in Oscillatory Gas Flow. *Phys. Rev. E* **78:** 026706. http://dx.doi.org/10.1103/PhysRevE.78.026706.

Tang, G., Tao, W., and He, Y. 2005. Thermal Boundary Condition for the Thermal Lattice Boltzmann Equation. *Phys. Rev. E* **72:** 016703. http://dx.doi.org/10.1103/PhysRevE.72.016703.

Wang, F.P., and Reed, R.M. 2009. Pore Networks and Fluid Flow in Gas Shales. Paper SPE 124253 presented at the SPE Annual Technical Conference and Exhibition, New Orleans, Louisiana, 4–7 October. http://dx.doi.org/10.2118/124253-MS.

Zhou, J.G. 2004. *Lattice Boltzmann Methods for Shallow Water Flows*. New York: Springer Verlag.

Ebrahim Fathi is an assistant professor of petroleum engineering at West Virginia University. Fathi holds BS and MSc degrees from Tehran University and his PhD degree in petroleum engineering from the University of Oklahoma. Fathi's research interests are unconventional reservoir engineering and natural-gas production, multiscale reservoir simulation, and upscaling of the fluid flow, transport, and reaction processes in heterogeneous porous media.

I. Yucel Akkutlu is an associate professor of petroleum engineering at the Texas A&M University. His current academic research is on thermodynamics of fluids in nanoporous materials, and on scaling up and homogenization of coupled transport and reaction processes in low-permeability geological formations exhibiting multiscale pore structures. Akkutlu holds MSc and PhD degrees in petroleum engineering from the University of Southern California. He currently serves the Natural Sciences and Engineering Research Council of Canad as a member of the Materials and Chemical Engineering Committee. Akkutlu is the Executive Editor of the *SPE Journal.*